Supporting Information

3D Narrow-Bandgap Perovskite Semiconductor Ferroelectric

Methylphosphonium Tin Triiodide for Potential Photovoltaic Application

Han-Yue Zhang,* Ren-Gen Xiong

Correspondence to: zhanghanyue@seu.edu.cn

Materials and Methods

Synthesis

Dichloro(methyl)phosphine: The synthetic procedure has been slightly modified from that in ref. 1. Anhydrous aluminum chloride (0.57 mol) was added in a three-necked flask equipped with a T-junction. The reaction system was subjected to three times of repeated vacuum and nitrogen filling. Then phosphorus trichloride (0.5 mol) was syringed into the flask and the mixture was heated at 70 °C for 1 hour. After cooling, methyl iodide (0.5 mol) was added dropwise over 0.5 hour at -10 °C. The reaction solution solidified gradually over the next 3-5 hours and further stirring was impossible. Then, dry potassium chloride (0.57 mol) and iron powder (30 g) were added to the solid complex. The reaction mixture was distilled to collect the fraction containing iodine/dichloro(methyl)phosphine at 80-165 °C. The mixture was then fractionated to give pure dichloro(methyl)phosphine as a colorless liquid, yield: 30%, b.p. 80-82 °C.

Methylphosphonium iodide: 4.2 g of dichloromethylphosphine was added to 33 ml of dichloromethane. Then, 3 g of ethylene glycol was added dropwise at room temperature. The violent exothermic reaction occurred immediately, accompanied by the formation of HCl gas. At the same time, colorless crystals continuously appeared on the sublimator, which is methylphosphonium chloride. When the colorless crystals no longer increase, dissolved them in hydroiodic acid solution and stored above in the refrigerator. Large quantities of crystals precipitated out at the bottom of the bottle, i.e. methylphosphonium iodide (MPI), with a yield of 20%.[2] ^{1}H NMR (300 MHz, CD$_3$CN) δ 3.59 (s, 3H); ^{13}C NMR (75 MHz, CD$_3$CN) δ 118.36; ^{31}P NMR (121 MHz, CD$_3$CN) δ -164.82 (Figure S1 and Figure S2).

Crystal growth: Black block crystals of MPSnI$_3$ were collected from a hydroiodic acid solution with equimolar amounts of MPI and SnI$_2$ by the temperature cooling method (1 degree per day) in an Argon atmosphere.

Crystal structure determination

Crystallographic data were collected using a Rigaku Saturn 924 diffractometer equipped with

temperature control device, by using Mo Kα (λ = 0.71075 Å) radiation. Data processing including empirical absorption correction, cell refinement, and data reduction was performed using the Crystal Clear software package. CCDC 2031849-2031850, and 2036182 for the compounds contain the supplementary crystallographic data for this paper. These data can be obtained free of charge from the Cambridge Crystallographic Data Centre via www.ccdc.cam.ac.uk/data_request/cif. The data collection and structure refinement of these crystals are summarized in Table S1.

Characterization methods

Common characterization methods like differential scanning calorimetry (DSC), powder X-ray diffraction (XRD), second harmonic generation (SHG) and dielectric measurements were described elsewhere.[3, 4]

UV-vis diffuse-reflectance spectra measurements were performed at room temperature using a Shimadzu UV-3600Plus spectrophotometer mounted with ISR-603 integrating sphere operating from 200 to 1100 nm. $BaSO_4$ was used as a 100% reflectance reference. Powdered crystal of $MPSnI_3$ was prepared for measurement. The generated reflectance-versus-wavelength data were used to estimate the band gap of the material by converting reflectance data to absorbance according to the Kubelka−Munk equation: $F(R_\infty) = (1- R_\infty)^2/2R_\infty$. Therefore, the optical band gap can be determined by the variant of the Tauc equation:

$$(h\nu \cdot F(R_\infty))^{1/n} = A(h\nu - E_g), \text{ Where:}$$

h: Planck's constant, ν: frequency of vibration, $F(R_\infty)$: Kubelka−Munk equation, E_g: band gap, A: proportional constant. The value of the exponent n denotes the nature of the sample transition. For direct allowed transition, n = 1/2; for indirect allowed transition, n = 2. Hence, the optical band gap E_g can be obtained from a Tauc plot by plotting $(h\nu \cdot F(R_\infty))^{1/n}$ against the energy in eV and extrapolation of the linear region to the X-axis intercept.

The Raman shifts were measured by the Raman spectrometer (Horiba, LabRAM HR Evolution) with a reflection method. The excitation laser was 532 nm. A 50 × microscope objectives were used to focus the excitation on the micrometer size samples. The spectrum was dispersed by a 600 groove per millimeter diffraction grating and accumulated 3 times with an exposing time of 2s.

PFM characterization

The PFM measurement was carried out on a commercial piezoresponse force microscope (Oxford instrument, Cypher ES) with high-voltage package and in-situ heating stage. PFM is based on the atomic force microscopy (AFM), with an AC drive voltage applied to the conductive tip. Conductive Ti/Ir-coated silicon probes (ASYELEC.01-R2, Oxford instrument) were used for domain imaging and polarization switching studies, with a nominal spring constant of ~2.8 nN/nm and a free-air resonance frequency of ~75 kHz. Since the amplitude of the low-frequency vertical PFM was within the noise level of the quadrant photodetector of the AFM, we performed the PFM experiments at contact resonance. The typical drive frequency was in the range of 330 to 360 kHz for vertical image and 870 to 900 kHz for lateral image, depending on the contact resonant frequency.

Calculation condition

The first-principles calculations were performed within the framework of density functional theory implemented in the Vienna ab initio Simulation Package (VASP).[5, 6] The energy cut-off for the expansion of the wave functions was fixed to 550 eV and the exchange−correlation interactions were treated within the generalized gradient approximation of the Perdew−Burke−Ernzerhof type.[7] For the integrations over the k-space we used a 4x4x4 k-point mesh. The experimental crystal structure was used as the ground state for evaluating the ferroelectric polarization. The rotation and displacement of the MA and MP cations are realized by matrix transformation of the coordinates using Microsoft Excel.

Perovskite film deposition

$FASnI_3$ perovskite film was prepared by one-step method. $FASnI_3$ complex solution was prepared by dissolving FAI and SnI_2 in DMSO at the molar ratio of 1:1. After the complex solution was stirred for 1 hour, the perovskite solution was added dropwise to the prepared PEDOT:PSS substrate, and then the solution was spin-coated at 5000 rpm for 90 s, and the anti-solvent chlorobenzene was dropped on the spinning substrate during the spin-coating process. After that, the perovskite films were annealed at 70 °C for 30 min. $MASnI_3$ perovskite film was also prepared by one-step method. $MASnI_3$ complex solution was prepared by dissolving MAI and SnI_2 (molar ratio is 1:1) in mixed solvents DMF:DMSO (V_{DMF}/V_{DMSO} is 3:1). After the complex solution was stirred for 1 hour, the perovskite solution was added dropwise to the prepared PEDOT:PSS substrate, and then the solution was spin-coated at 4000 rpm for 60 s, and the anti-solvent CB was dripped onto the spin-coating film. After that, the perovskite films were annealed at 70 °C for 30 min. $MPSnI_3$ perovskite films were prepared by vapor assisted solution process method. Firstly, SnI_2 was dissolved in a mixed solution of DMF and DMSO (V_{DMF}/V_{DMSO} is 3:1) with molar concentration of 1 $_M$ and stirred for 1 hour. The SnI_2 films were prepared by spin-coating its precursor solution at 4000 rpm for 40 s on PEDOT:PSS substrate and annealing at 70 °C for 1 min. Then, the prepared SnI_2 films and 30 mg of new materials were put into a glassware together and kept at 70 °C for several minutes. The two components would react with each other to form $MPSnI_3$ perovskite, which can be confirmed by the powder XRD patterns for $MPSnI_3$ perovskite film in Figure S13.

Device fabrication and Characterization

Firstly, the ITO substrate was cleaned by using surfactant, deionized (DI) water, acetone, isopropanol (IPA) and deionized (DI) water with ultrasonic cleaning for 15 minutes respectively, and then N_2 flow was used to dry the ITO. Then, oxygen plasma was used to further clean the ITO substrate for 15 minutes. After filtering PEDOT:PSS solution with a 0.45 μm filter, the PEDOT:PSS film was deposited by spin-coating PEDOT:PSS solution on ITO substrate at 4000 rpm for 40 s and annealing at 170 °C for 30 min. The perovskite films were deposited on the PEDOT:PSS substrate as described in the perovskite film deposition part. Finally, C60 (40nm), 2,9-dimethyl-4,7-diphenyl-1,10-phenanthroline (BCP) (5nm) and Ag (100 nm) electrodes were deposited by vacuum thermal deposition.

The $J–V$ curves of PSCs were measured using a Keithley 2602B source in the glove box filled with N_2 at room temperature under an intensity of 100mW/cm^2 at AM 1.5 G, calibrated by a standard Si solar cell (PVM937, Newport). The light source was a 450 W xenon lamp (Oriel solar simulator, 94023A). The PSCs active area (0.17 cm^2) was well defined by a mask, and further calibrated by microscopy. The $J–V$ curves were tested at reverse scan direction (from 0.5 V to -0.02 V, step 0.02 V) without any pre-conditioning before the test. For the stability measurement, the devices were aged in air with a relative humidity of 50% for 60, 120,180, and 300 minutes, respectively, and then tested in a glove box filled with N_2.
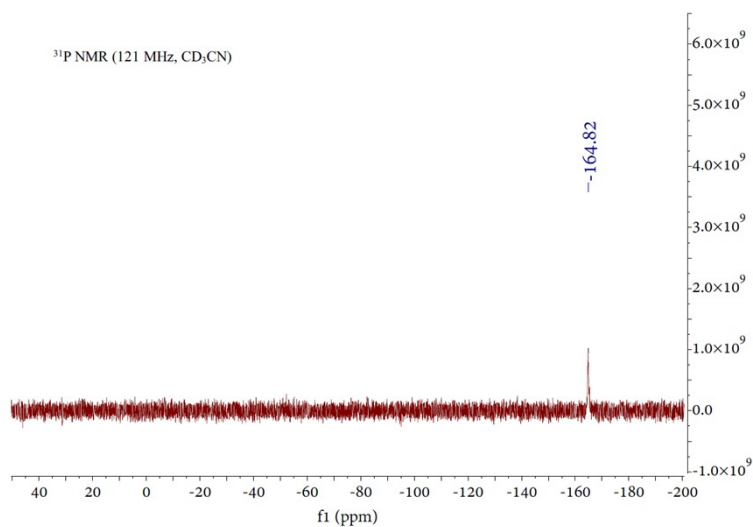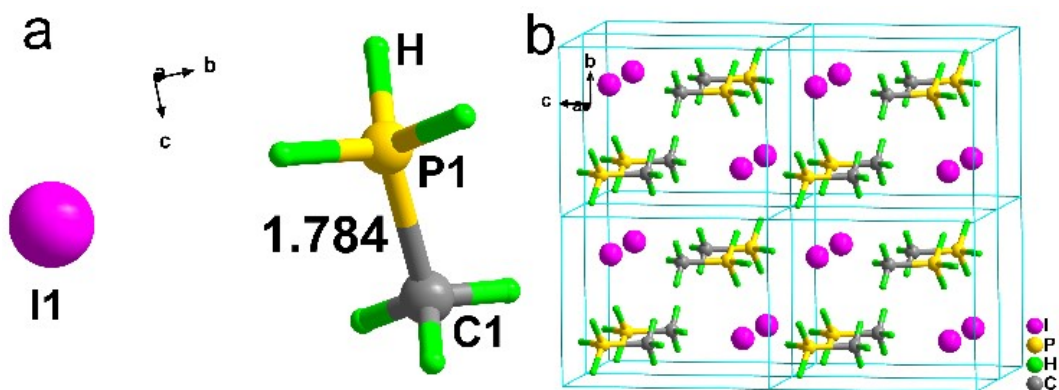
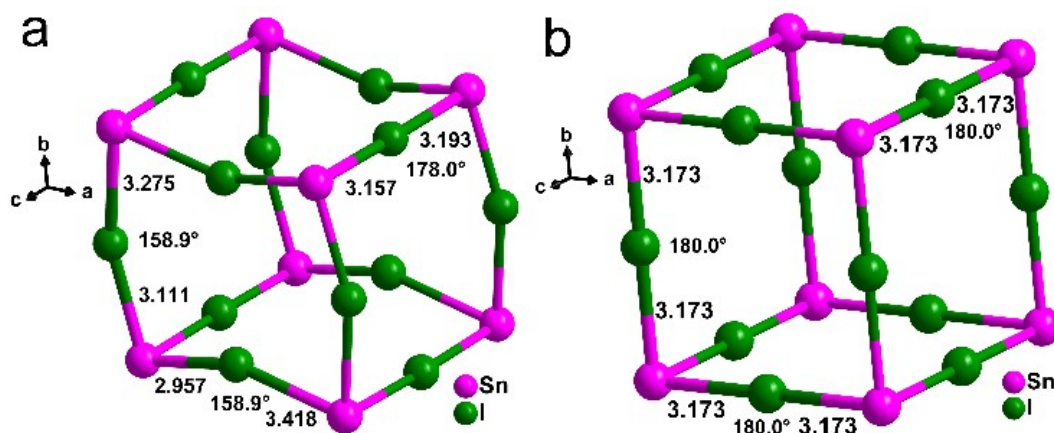**Figure S1.** The ^{31}P NMR spectrum of MP iodide.
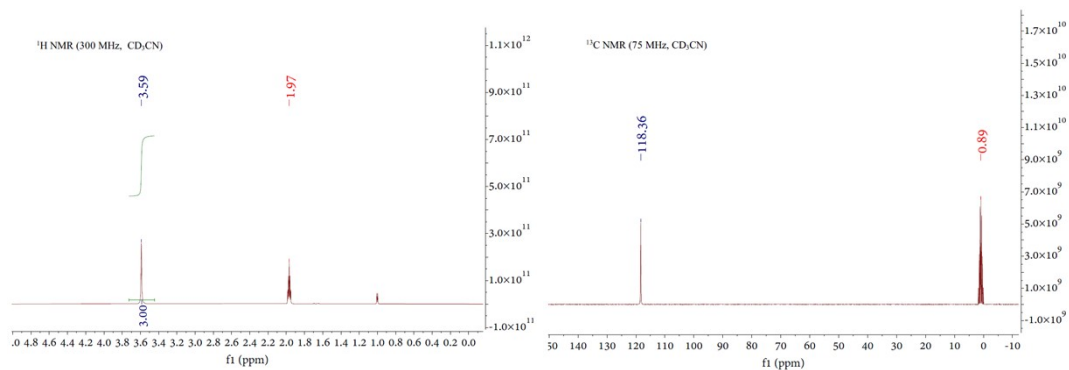
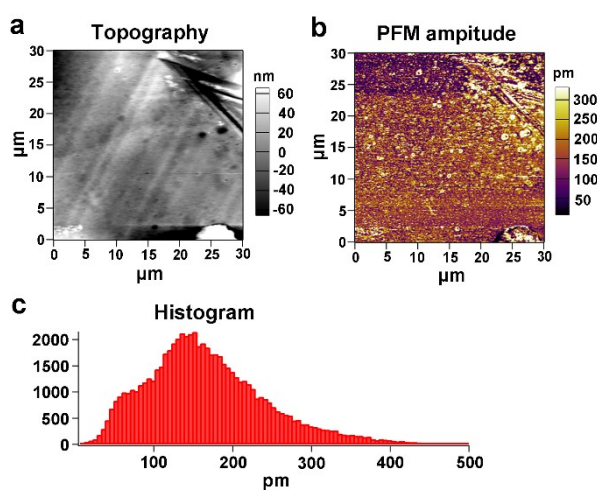**Figure S2.** The ^{1}H NMR (left) and ^{13}C NMR (right) spectra of MP iodide.
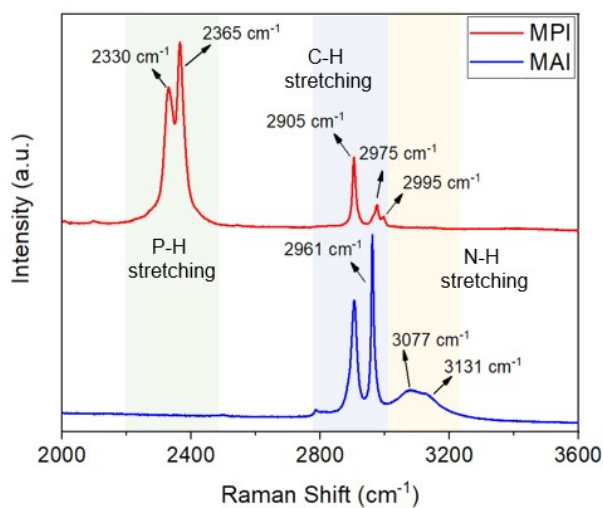
**Figure S3.** The Raman shifts of MPI and MAI at room temperature.

Figure S4. (a) The basic structures for MPI at 293 K. (b) The packing view of the structures for MPI at 293 K.

Figure S5. Selected Sn–I lengths (Å) and Sn–I–Sn angles (°) are labeled for MPSnI$_3$ at (a) 273 K, and (b) 313 K, respectively.

Figure S6. (a) Topography and corresponding (b) vertical PFM amplitude mapping obtained on the surface of MPSnI$_3$ crystal at 300 K. (c) The statistical histogram of vertical PFM amplitude signals.
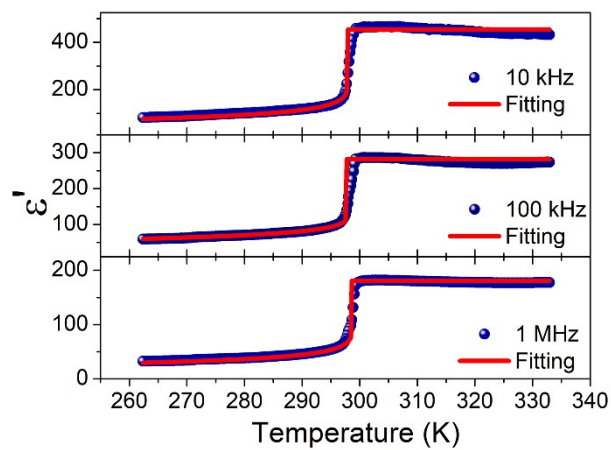
Figure S7. Fitting of the temperature-dependent real part of dielectric permittivity (ε') of MPSnI$_3$.

As shown in Figure S7, the dielectric permittivity ε as a function of temperature T across the improper ferroelectric phase transition point T_c is fitted by the Landau-Ginzburg theory proposed earlier.[8-10] The Landau energy density f is written as:

$$f = \frac{1}{2}\alpha(T-T_0)\eta^2 + \frac{1}{4}\beta\eta^4 + \frac{1}{6}\gamma\eta^6$$
$$+ \frac{1}{2}\varepsilon_0^{-1}P^2 + a_1\eta^2 P + a_2\eta^2 P^2 - EP \quad , \qquad (1)$$

where ($\alpha > 0$, β, $\gamma > 0$, $\varepsilon_0 > 0$, a_1, $a_2 > 0$) are the free energy constants in the polynomials, T_0 is the unstable limit of high-temperature paraelectric phase, η is the primary order parameter and P is the spontaneous polarization as the secondary order parameter, E is the electric field.

To determine the temperature dependences of $P(T)$ and $\eta(T)$, it is necessary to find the minimum of the Landau energy f with $E = 0$. The polarization P can be obtained from the following equilibrium conditions for both paraelectric phase and ferroelectric phase:

$$\frac{\partial f}{\partial \eta} = \alpha(T-T_0)\eta + \beta\eta^3 + \gamma\eta^5 + 2a_1\eta P + 2a_2\eta P^2 = 0 \quad , \quad (2)$$

and

$$\frac{\partial f}{\partial P} = \chi_0^{-1}P + a_1\eta^2 + 2a_2\eta^2 P = 0 \quad , \qquad (3)$$

In the high-temperature paraelectric phase, $P = 0$, $\eta = 0$, and $\varepsilon = \varepsilon_0$ which is a constant. This implies that the dielectric permittivity in the paraelectric phase is temperature-independent. For realistic improper ferroelectrics, the measured dielectric constant in the paraelectric phase region does show some weak temperature dependence. This difference is believed to originate from the assumption that only the first term in the right side of Eq.(1) is T-dependent in the Landau theory of phase transitions. We now discuss the ferroelectric phase. The inverse dielectric permittivity in the limit of low T ($< T_c$) and low electric field can be obtained:

$$\varepsilon^{-1} = \varepsilon_0^{-1} + 2a_2\eta^2 - \frac{2a_1^2}{(\beta+2\gamma\eta^2)(1+2a_2\chi_0\eta^2)^2} \quad , \qquad (4)$$

where $\eta(T)$ is determined by equation:

$$\alpha(T-T_0) + \beta\eta^2 + \gamma\eta^4 - \frac{2a_1^2\chi_0\eta^2}{1+2a_2\chi_0\eta^2} + \frac{2a_1^2 a_2\chi_0^2\eta^4}{\left(1+2a_2\chi_0\eta^2\right)^2} = 0 \quad , \quad (5)$$

For the present improper ferroelectric, it is clear that the paraelectric to ferroelectric phase transition is accompanied by abrupt jump of the dielectric permittivity at T_c. Since $a_2 > 0$, the T-dependence of η is:

$$\eta^2 = \frac{2}{3}\Delta\eta^2[1 + (\frac{T_1-T}{T_1-T_0})^{1/2}] \quad , \qquad (6)$$

where $\Delta\eta^2$ is the jump of η^2 at T_c. Here T_1 is defined by $T_1 = (4T_c - T_0)/3$.

Substituting Eq.(6) into Eq.(4), ignoring the last term on the right side of Eq.(4) results in the dielectric constant in the ferroelectric phase:

$$\varepsilon^{-1} = \varepsilon_0^{-1} + \frac{2}{3}\Delta\varepsilon^{-1}[1+(\frac{T_1-T}{T_1-T_0})^{1/2}]$$

$$\Delta\varepsilon^{-1}=2a_2\Delta\eta^2 \qquad\qquad\qquad (7)$$

It is clear that the dielectric permittivity will increase with increasing T in the ferroelectric phase region, and a jump of ε at T_c up to a larger value will occur, as observed for most improper ferroelectrics.[11]

Eq.(7) is then used to fit the measured dielectric permittivity as a function of T below T_c, while the dielectric constant at $T > T_c$ would be a constant.
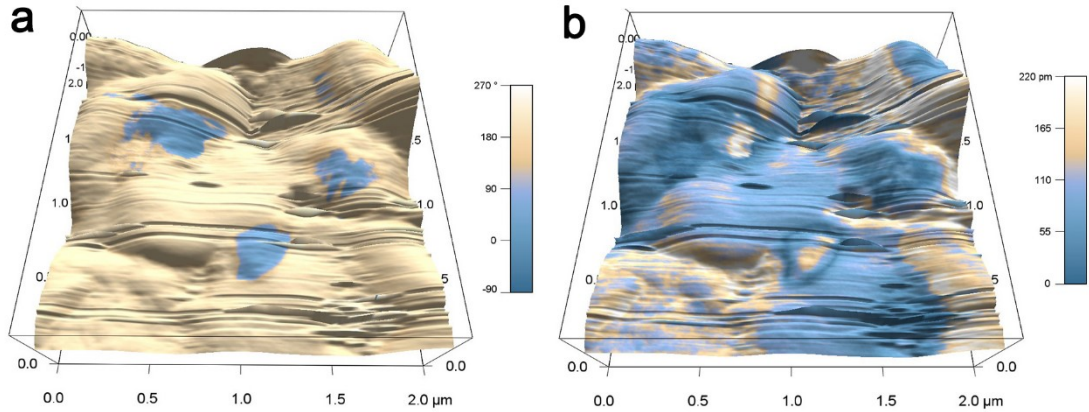

Figure S8. Vertical PFM phase mapping (a) and amplitude mapping (b) overlaid on 3D topography in the single crystal of MPSnI$_3$.
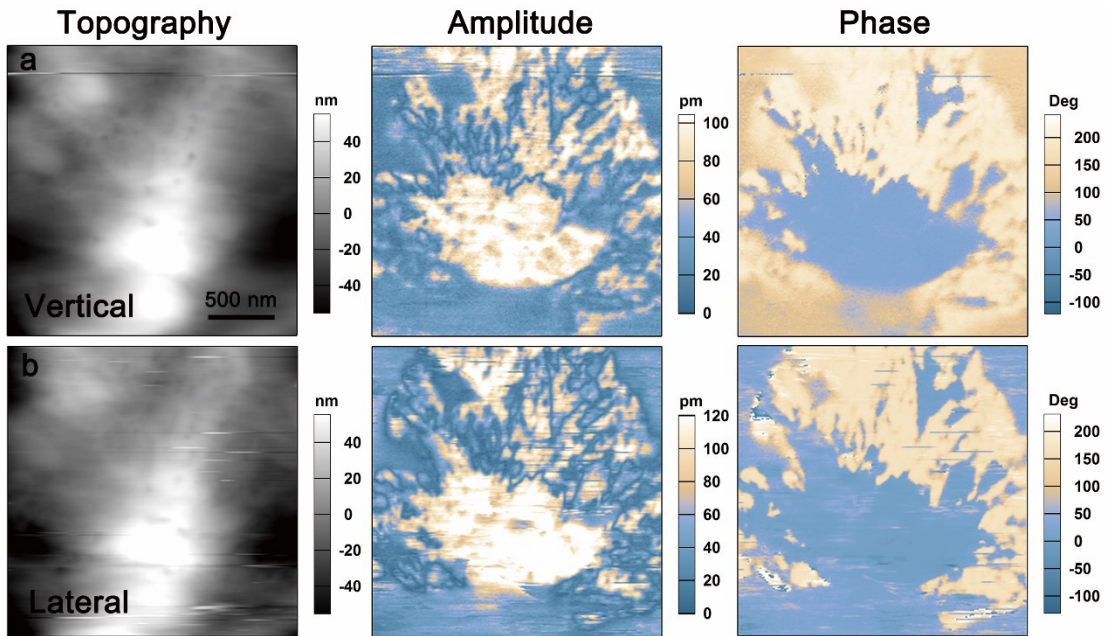

Figure S9. Topographic images, and vertical (a) and lateral (b) PFM phase and amplitude images of the crystal surface for MPSnI$_3$ at 288 K.
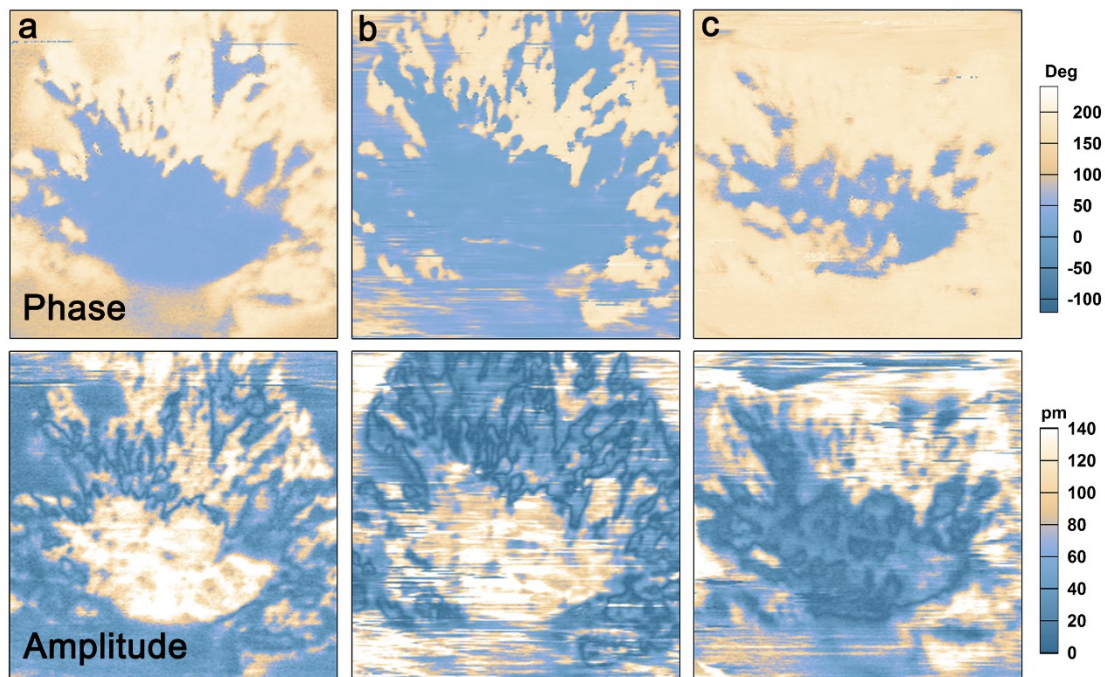
Figure S10. Vertical PFM phase (top) and amplitude (bottom) images of the crystal surface for MPSnI$_3$ at 288 K. (a) Initial state. (b) After the first switching with negative bias at -40 V. (c) After the succeeding switching with positive bias at +50 V. The blue and yellow contrasts in phase images represent the polarizations oriented upward and downward, respectively.
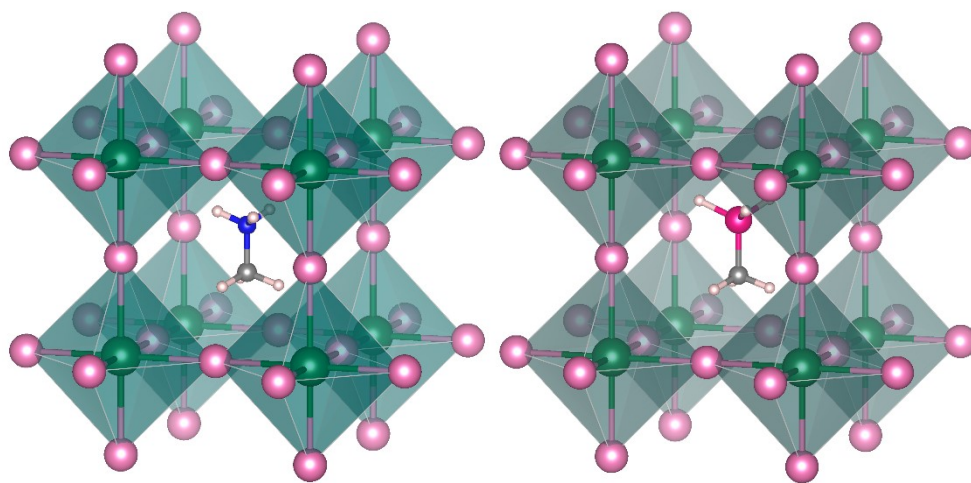

**Figure S11.** The structural model of MASnI$_3$ and MPSnI$_3$ used to calculate the molecular rotation barrier.
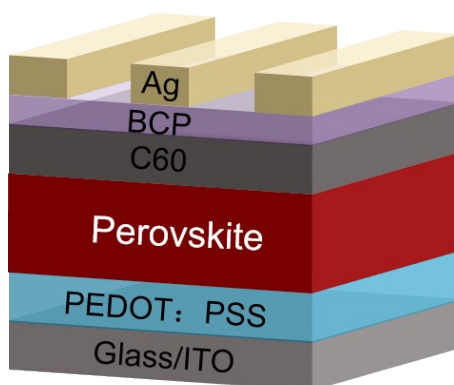
Figure S12. Device structure of MPSnI$_3$, FASnI$_3$, or MASnI$_3$ PSCs.
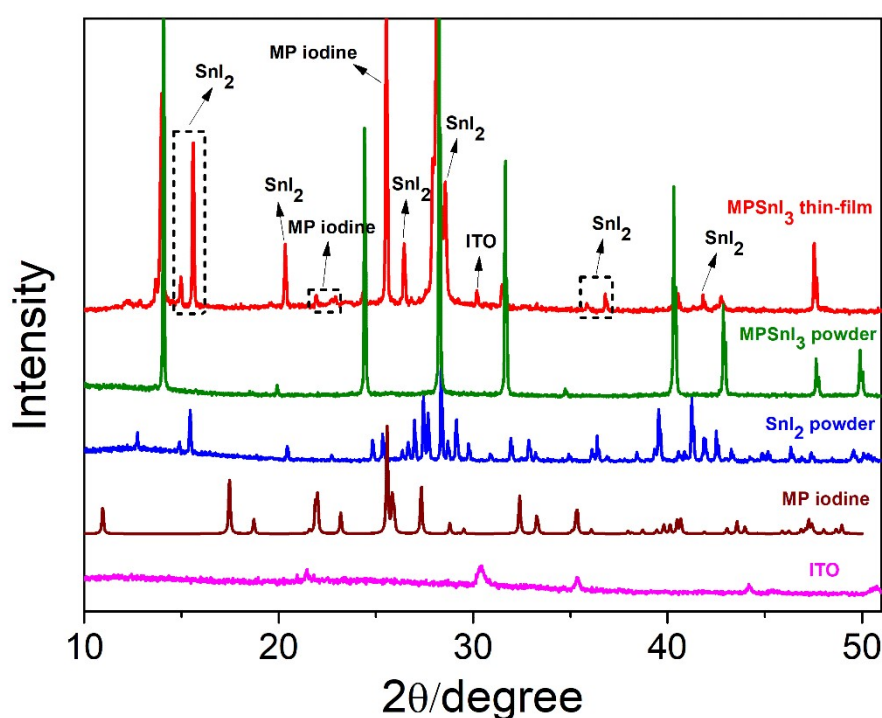
**Figure S13.** The powder XRD pattern for MPSnI$_3$ perovskite film on ITO-coated substrate. MPSnI$_3$ perovskite film was fabricated by vapor assisted solution process. Firstly, the precursor solution of 1M molar concentration was prepared by dissolved SnI$_2$ in a mixed solution of DMF and DMSO (V$_{DMF}$/V$_{DMSO}$ is 3:1) with molar concentration of 1 M and stirred for 1 hour. Then the SnI$_2$ film was deposited by spin-coating the precursor solution on PEDOT:PSS substrate at 4000 rpm for 40 s and annealing at 70 ºC for 1 min. Finally, the prepared SnI$_2$ film and 30 mg of the MPI were put into a glassware together and kept at 70 ºC for several minutes. The MPI would react with SnI$_2$ to form MPSnI$_3$ perovskite.
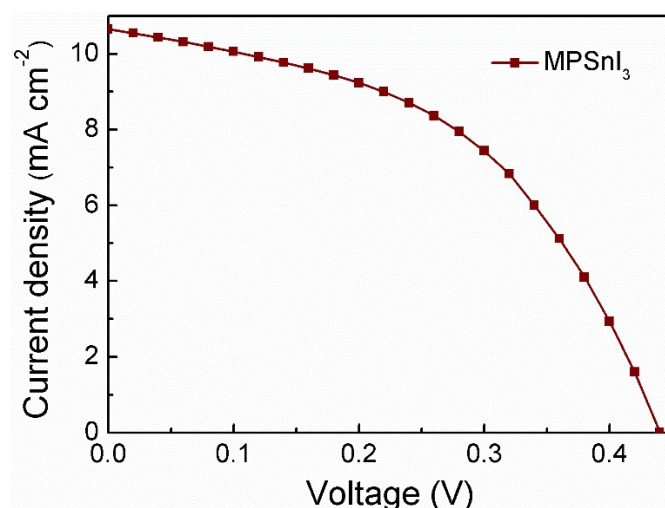
Figure S14. *J-V* curve of the MPSnI₃ champion device. MPSnI₃ perovskite solar cell achieved a power conversion efficiency of 2.231% without SnF₂.
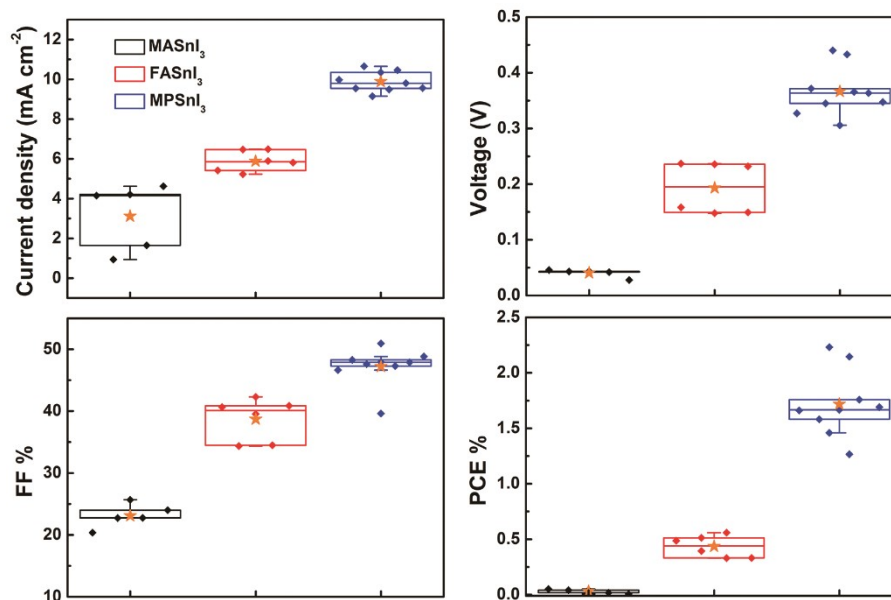
Figure S15. Statistics of J_{sc}, V_{oc}, FF(%) and PCE(%) parameters of MASnI₃, FASnI₃ and MPSnI₃ PSCs, respectively. All the PSCs have the same device structure of ITO/PEDOT:PSS/perovskite/C60/BCP/Ag without any additives like SnF₂ in the perovskites.
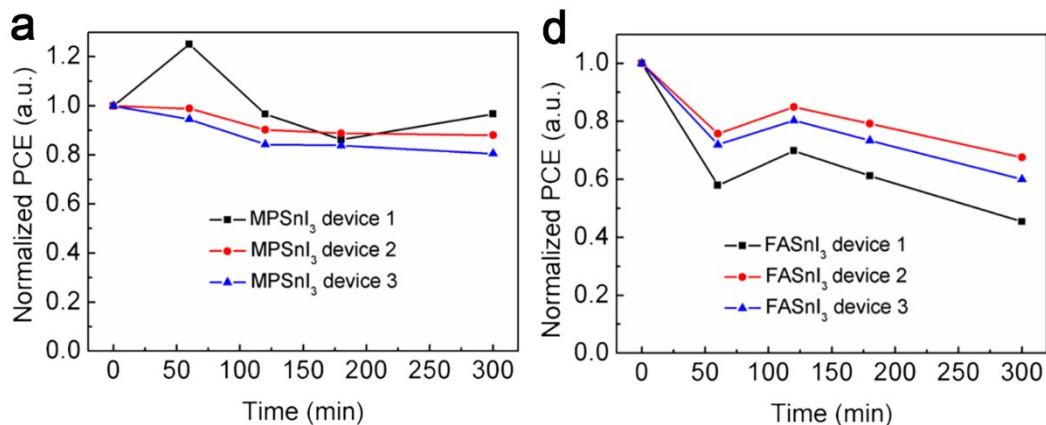
Figure S16. Stability of FASnI$_3$ and MPSnI$_3$ devices in air at room temperature. The stabilities of FASnI$_3$ and MPSnI$_3$ devices are tested under 50% relatively humidity in air. FASnI$_3$ devices 1, 2 and 3 represent three individual FASnI$_3$ perovskite solar cells with the same fabrication method, and MPSnI$_3$ devices 1, 2 and 3 are also three individual MPSnI$_3$ perovskite solar cells with the same fabrication method. Obviously, the MPSnI$_3$ devices exhibited slightly decreased PCE after 300 min, while the PCE of FASnI$_3$ devices was decreased significantly. The MPSnI$_3$ devices showed a better humid stability than FASnI$_3$ devices.
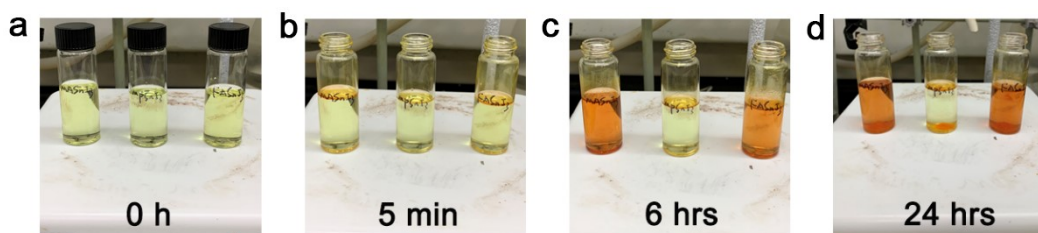
Figure S17. Stability of MASnI$_3$ (left), MPSnI$_3$ (middle) and FASnI$_3$ (right) solutions in the ambient condition. The stabilities of MASnI$_3$, MPSnI$_3$ and FASnI$_3$ solutions are tested under 80%-90% relatively humidity in air at room temperature. After 6 hours, MASnI$_3$ and FASnI$_3$ solutions began to deteriorate, from pale yellow to brown, while MPSnI$_3$ solution remained the same. And MPSnI$_3$ solution began to deteriorate after 24 hours, which showed a better stability than MASnI$_3$ and FASnI$_3$ solutions.

Table S1. Crystal data and structure refinement for MPSnI$_3$ at 273 K, and 313 K, and MPI at 293 K, respectively.

	273 K	313 K	293 K
Empirical formula	CH$_3$PH$_3$SnI$_3$	CH$_3$PH$_3$SnI$_3$	CH$_3$PH$_3$I
Formula weight	548.44	548.44	175.93
Crystal system	Orthorhombic	Cubic	Monoclinic
Space group	*Pba*2	*P$\bar{4}$3m*	*P*2$_1$/*m*
a (Å)	12.5156(8)	6.3464(2)	4.7369(4)
b (Å)	12.5460(8)	6.3464(2)	6.5201(5)
c (Å)	6.3490(4)	6.3464(2)	8.0744(7)
α (deg)	90	90	90
β (deg)	90	90	90.914(8)
γ (deg)	90	90	90
Volume (Å^3), *Z*	996.92(11), 4	255.61(2), 1	249.35(4), 2
D_{calcd} / g cm^{-3}	3.654	3.523	2.343
μ (mm^{-1})	11.927	11.628	6.541
F(000)	944	230	160
Goodness-of-fit on F^2	1.000	1.266	1.000
R_1 [a] (> 2σ)	0.1021	0.0520	0.0238
wR_2 [b] (> 2σ)	0.2525	0.1557	0.0552

[a]$R_1 = \Sigma||F_o| - |F_c||/\Sigma|F_o|$, [b]$wR_2 = [\Sigma(|F_o|^2 - |F_c|^2) / \Sigma|F_o|^2]^{1/2}$

Table S2. Selected bond lengths [Å] and angles [°] for MPSnI$_3$ at 273 K and 313 K, respectively.

273 K

Sn(1)-I(1)	3.112(5)	I(1)-Sn(1)#4	3.275(5)
Sn(1)-I(2)	2.957(5)	I(2)-Sn(1)#2	3.418(5)
Sn(1)-I(3)	3.157(10)	I(3)-Sn(1)#3	3.193(10)
I(2)-Sn(1)-I(1)	94.85(13)	I(3)-Sn(1)-I(3)#1	178.03(19)
I(2)-Sn(1)-I(3)	89.0(3)	Sn(1)-I(3)-Sn(1)#2	178.03(19)
I(1)-Sn(1)-I(3)	88.9(3)	Sn(1)-I(2)-Sn(1)#3	158.86(16)
I(1)-Sn(1)-I(3)#1	89.5(2)	Sn(1)-I(1)-Sn(1)#4	158.89(16)

313 K

Sn(1)-I(1)	3.1732(1)	Sn(1)-I(1)#6	3.1732(1)
Sn(1)-I(1)#5	3.1732(1)	Sn(1)-I(1)#1	3.1732(1)
Sn(1)-I(1)#2	3.1732(1)	I(1)-Sn(1)#7	3.1732(1)
I(1)#4-Sn(1)-I(1)	90.0	I(1)#5-Sn(1)-I(1)#6	90.0
I(1)#4-Sn(1)-I(1)#5	90.0	I(1)-Sn(1)-I(1)#1	90.0
I(1)#6-Sn(1)-I(1)#1	90.0	I(1)#5-Sn(1)-I(1)#1	90.0
I(1)#4-Sn(1)-I(1)#2	90.0	I(1)#2-Sn(1)-I(1)#1	90.0
I(1)-Sn(1)-I(1)#2	90.0	I(1)-Sn(1)-I(1)#6	90.0
I(1)#5-Sn(1)-I(1)#2	90.0	I(1)#4-Sn(1)-I(1)#6	90.0
I(1)#2-Sn(1)-I(1)#6	180.0	Sn(1)#7-I(1)-Sn(1)	180.0
I(1)#4-Sn(1)-I(1)#	180.0	I(1)-Sn(1)-I(1)#5	180.0

Symmetry transformations used to generate equivalent atoms, **For 273 K:** #1 x, y, z+1; #2 x, y, z-1; #3 1/2+x, 1/2-y, z; #4 1/2-x, 1/2+y, z; **For 313 K:** #1 y, z, x; #2 z, x, y; #3 -x, y, -z; #4 y+1, z, x; #5 x, y+1, z; #6 z, x, y+1; #7 x, y-1, z.

Table S3. Performance parameters of different perovskite devices.

	J_{sc} (mA cm^{-2})	V_{oc} (V)	FF (%)	PCE (%)
MASnI$_3$	3.113	0.040	23.096	0.031
FASnI$_3$	5.880	0.193	38.700	0.436
MPSnI$_3$	9.883	0.366	47.229	1.718

References

(1) Soroka M. A Simple Preparation of Methylphosphonous Dichloride. *Synthesis* **1977**, 77, 450.

(2) Fluck E.; Svara J.; Neumüller B.; Riffel H.; Thurn H. Darstellung und Struktur von Methylphosphoniumchlorid. *Z. Anorg. Allg. Chem.* **1986**, 536, 129-136.

(3) Liao, W. Q.; Zhang, Y.; Hu, C. L.; Mao, J. G.; Ye, H. Y.; Li, P. F.; Huang, S. D.; Xiong, R. G. A lead-halide perovskite molecular ferroelectric semiconductor. *Nat. Commun.* **2015,** 6, 7338.

(4) Zhang, H. Y.; Song, X. J.; Chen, X. G.; Zhang, Z. X.; You, Y. M.; Tang, Y. Y.; Xiong, R. G. Observation of Vortex Domains in a Two-Dimensional Lead Iodide Perovskite Ferroelectric. *J. Am. Chem. Soc.* **2020**, 142, 4925-4931.

(5). Kresse G.; Furthmüller J. Efficient iterative schemes for ab initio total-energy calculations using a plane-wave basis set. *Phys. Rev. B* **1996**, 54, 11169-11186.

(6) Kresse G.; Furthmüller J. Efficiency of ab-initio total energy calculations for metals and semiconductors using a plane-wave basis set. *Comput. Mater. Sci.* **1996**, 6, 15-50.

(7) Perdew J. P.; Burke K.; Ernzerhof M. Generalized Gradient Approximation Made Simple. *Phys. Rev. Lett.* **1996**, 77, 3865-3868.

(8) Dvorak V. Improper Ferroelectrics. *Ferroelectrics* **1974**, 7, 1-9.

(9) Kobayashi J.; Sato Y.; Enomoto Y. A phenomenological theory of dielectric and mechanical properties of improper ferroelectric crystals. *Phys. Status Solidi B-Basic Solid State Phys.* **1972**, 50, 335-343.

(10) Shaulov A.; Smith W. A.; Schmid H. DIELECTRIC ANOMALIES IN BORACITES. *Ferroelectrics* **1981**, 34, 219-225.

(11) You, Y.-M.; Liao, W.-Q.; Zhao, D.; Ye, H.-Y.; Zhang, Y.; Zhou, Q.; Niu, X.; Wang, J.; Li, P.-F.; Fu, D.-W.; Wang, Z.; Gao, S.; Yang, K.; Liu, J.-M.; Li, J.; Yan, Y.; Xiong, R.-G. *Science* **2017**, 357, 306.